

CUPID: Generative 3D Reconstruction via Joint Object and Pose Modeling

Binbin Huang^{†,1,2} Haobin Duan^{†,1,2} Yiqun Zhao^{1,2} Zibo Zhao³ Yi Ma^{1,2} Shenghua Gao^{†,1,2}

¹The University of Hong Kong ²Transcengram ³Tencent

<https://cupid3d.github.io>

Abstract

We introduce CUPID, a generative 3D reconstruction framework that jointly models the full distribution over both canonical objects and camera poses. Our two-stage flow-based model first generates a coarse 3D structure and 2D-3D correspondences to estimate the camera pose robustly. Conditioned on this pose, a refinement stage injects pixel-aligned image features directly into the generative process, marrying the rich prior of a generative model with the geometric fidelity of reconstruction. This strategy achieves exceptional faithfulness, outperforming state-of-the-art reconstruction methods by over 3 dB PSNR and 10% in Chamfer Distance. As a unified generative model that decouples the object and camera pose, CUPID naturally extends to multi-view and scene-level reconstruction tasks without requiring post-hoc optimization or fine-tuning.

1. Introduction

Inferring an object’s 3D structure from a single 2D image is a fundamental challenge in computer vision. Consider the physics of image formation: $\mathbf{I} = \mathcal{P}(\mathcal{O}, \theta)$, where \mathbf{I} is the rendered image, \mathcal{O} is the 3D object in an *object-centric, view-agnostic* canonical frame, θ is the camera pose in that frame, and $\mathcal{P}(\cdot, \cdot)$ projects the 3D object onto the image. Since object and pose jointly determine \mathbf{I} , given a single image, it is extremely challenging to disentangle the intrinsic properties of object \mathcal{O} (e.g., shape and texture) from the extrinsic property of the partial observation, namely the camera viewpoint θ .

Current approaches often tackle this problem from only one aspect. On one hand, **3D generative models** [24, 31, 59, 70, 72] excel at generating a high-quality canonical 3D object \mathcal{O} , while completely ignoring the camera pose θ , a crucial component of image formation. As a result, contemporary image-conditioned 3D generators typically produce plausible *variations*, but struggle to achieve a *faithful reconstruction* consistent with the input view, leading to shape

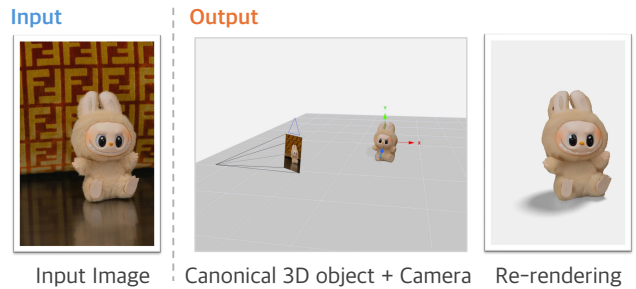


Figure 1. **Generative 3D reconstruction from a single image.** Left: Input image. Middle: Our method recovers a canonical 3D model (intrinsic properties such as shape and texture) along with the exact camera pose (extrinsic property) that generated the input. Right: Re-rendering the 3D model from the estimated pose faithfully reproduces the input.

inconsistencies and color drift, especially when real-world inputs deviate from the training distribution. Furthermore, integrating generated 3D assets into complex scene reconstruction is highly challenging, requiring costly and fragile post-hoc optimization for spatial alignment [8, 12, 65]. The difficulty arises primarily from the missing camera pose prior, which is never modeled in these approaches.

On the other hand, common **3D reconstruction methods** [39, 48, 51, 53, 64] produce 3D geometry through 2D-to-3D lifting in a *pixel-aligned, view-centric* frame, which essentially fixes the camera pose θ as an identity constant. As a result, they lack the generative ability to plausibly “imagine” occluded regions, yielding incomplete models or collapsing the scene into a single, undifferentiated mesh even given sufficient views [48, 51, 53]. Although some methods [16, 49] attempt to deterministically complete unseen regions, learning such an entangled data distribution limits their ability to truly “understand” the underlying 3D spatial relationship that is crucial to embodied AI.

Observing the gap between these two lines of work, we argue an ideal system should **jointly model both components within a unified framework**, deriving this joint distribution from a large set of 2D observations without fixing camera pose as identity or specifying how the canonical

[†] Equal contribution. [‡] Corresponding author

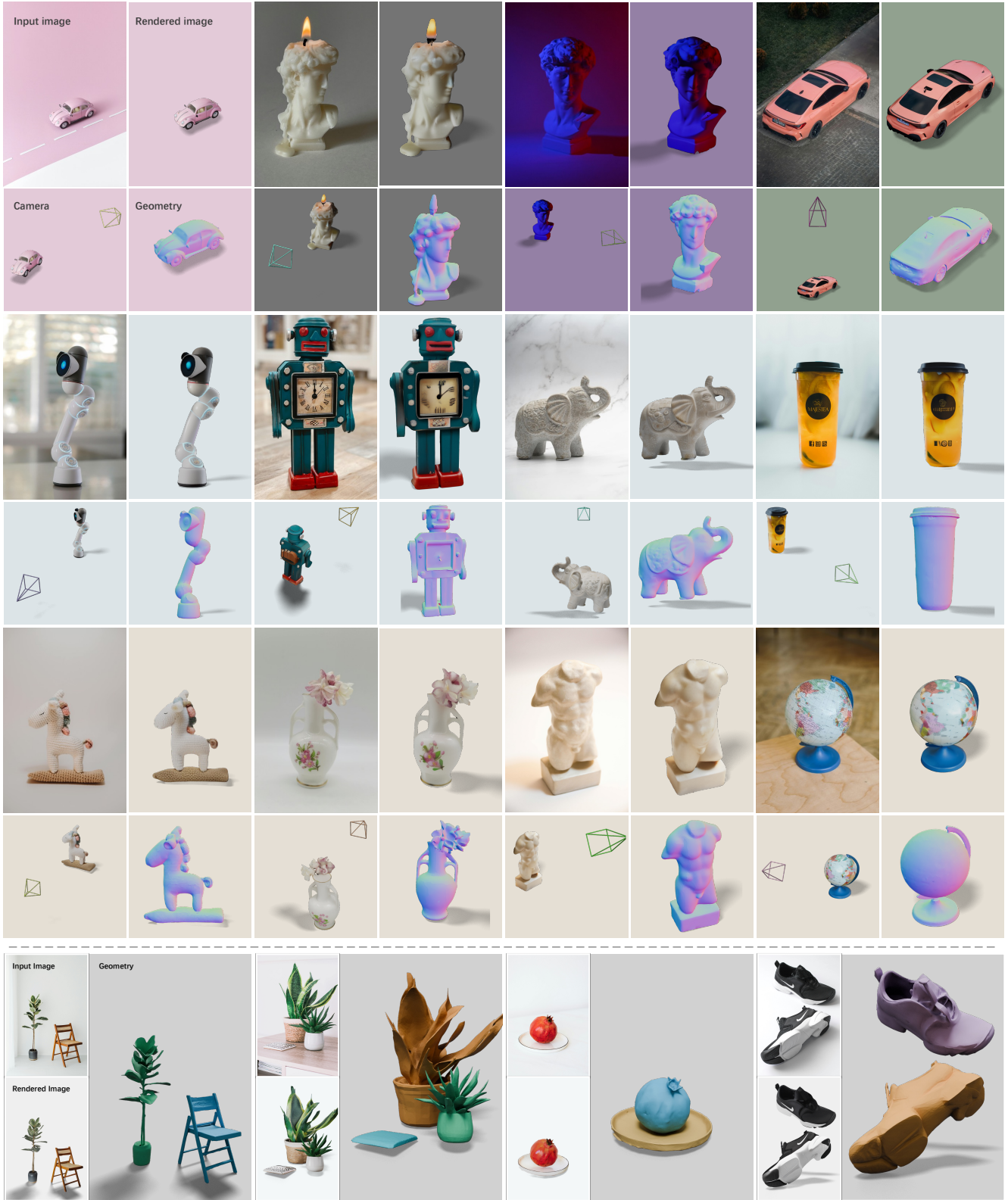


Figure 2. **Results for generative 3D reconstruction from a single test image.** Given an input image (top left), CUPID estimates camera pose (bottom left) and reconstructs 3D model (bottom right), re-rendering the input (top right). It is robust to changes in scale, placement, and lighting while preserving fine details, and supports component-aligned scene reconstruction (bottom row). All results are produced in seconds via feed-forward sampling of the learned model. See [cupid3d.github.io](https://github.com/cupid3d) for an immersive view of the interactive 3D results.

object is oriented*. This mirrors how humans perceive the world: as illustrated in Fig. 1, we readily infer that the image captures the plush toy from its left frontal side. This implies that, through exposure to abundant visual data, we maintain a view-agnostic mental impression of 3D objects while simultaneously recalling viewpoint that would most reproduce a given 2D observation. This formulation essentially bridges 3D reconstruction and 3D generation into a unified task, which we call **Generative 3D Reconstruction**.

To this end, we introduce CUPID (for “in-CUbe Pixel Distribution”), a probabilistic reconstruction framework designed to achieve this synthesis by simultaneously generating a full 3D object \mathcal{O} and reasoning the exact camera pose θ that can *faithfully* reproduce the 2D observation. CUPID formulates reconstruction as a conditional sampling process within a unified flow-based model that operates in two stages. First, it jointly generates a coarse 3D structure and a dense field of 3D-to-2D correspondences, enabling camera pose recovery through a simple PnP solver [1]. Second, conditioned on this recovered pose, a refinement stage injects *pixel-aligned features* from the input image directly into the generative process. This novel conditioning mechanism enforces consistency with the visual evidence, marrying the rich prior of a generative model with the geometric fidelity of reconstruction. As Fig. 2 shows, this simple yet effective approach produces geometrically complete 3D reconstructions that are texturally faithful to the input image.

The primary contributions of this work can be summarized as follows:

- **A unified generative reconstruction framework.** CUPID bridges 3D generation and reconstruction by jointly modeling a canonical 3D object and camera pose. This unified design excels at single-view reconstruction, and can be applied to multi-view and component-aligned scene reconstruction without task-specific tuning or optimization.
- **A novel pose-conditioned refinement strategy.** Our two-stage approach uses the recovered pose to inject pixel-local features, a mechanism critical for achieving high-fidelity reconstructions free from the shape and color inconsistencies typical of generative models.
- **Strong object-level reconstruction performance.** CUPID leverages its generative capabilities to set a new standard in reconstruction fidelity, outperforming top holistic reconstruction models [16] by over 3 dB PSNR while matching the geometric accuracy of state-of-the-art monocular estimators [48, 51].

*3D artist-curated training data is typically placed in a display-ready frame that naturally encodes human priors on canonicalness. Our learned representation captures this dominant mode without explicit labeling.

2. Related Work

3D reconstruction from many images. Complete 3D reconstruction traditionally requires multiple views and Structure-from-Motion [39, 40]. DUST3R [53] predicts pixel-aligned point maps for image pairs, enabling efficient recovery of view-centric camera poses and partial geometry; subsequent works improve efficiency and flexibility [3, 19, 28, 48, 50, 52, 63, 64, 71]. CUT3R processes images recurrently [50]; VGGT jointly predicts depth, point maps, and poses [48]; and MoGe introduces affine-invariant point maps for monocular geometry [51]. These approaches lack generative capabilities and cannot plausibly infer occluded regions, resulting in partial geometry from limited input views. Even with abundant views, they produce a single fused scene without object separation. In contrast, our method models a joint distribution over 3D objects and camera pose, enabling completion of partial observations into fully compositional, object-level scenes.

3D reconstruction from one or a few images. High-quality multiview data are hard to obtain in practice, motivating single- or sparse-view reconstruction with large models [26, 45, 46, 55, 60, 62, 67]. LRM [16] shows that complete 3D can be regressed from a single image under a fixed camera. PF-LRM [49] enables pose-free sparse-view reconstruction via differentiable PnP [5]. Subsequent work improves single-view quality by augmenting novel views from 2D generative priors and using more efficient representations [25, 61, 67] or architectures [4]. Yet their entangled *pixel-aligned* representations never decouple 3D content and viewpoint, typically assuming a fixed camera (e.g., unit focal length), making them poorly suited to real-world images with unknown camera parameters. Their deterministic formulations cannot model uncertainty in unseen regions, failing to produce plausible 3D variations. Our generative framework instead enables synthesizing diverse, high-fidelity 3D objects under flexible conditioning.

3D reconstruction from generative priors. Dreamfusion [33] pioneers 3D generation from 2D diffusion models [37, 38]. Zero-1-to-3 [27] and subsequent work [11, 15, 22, 29, 42, 54, 57] fine-tune image diffusion models for single image-to-3D generation. Recent methods [36, 43, 73] leverage video diffusion priors to achieve greater view consistency. Nevertheless, they rely on 2D generative priors that require dense supervision to reconstruct 3D objects and inherit the limitations of many-image-to-3D, most notably their difficulty in producing compositional scenes. Recent work [8, 17, 65] incorporate native 3D generative priors [59, 70] for scene reconstruction. Yet, without explicitly modeling camera pose, these methods resort to costly and fragile post-hoc optimization or additional tuning on spatial layouts [17]. Notably, CAST [65] designs a multi-

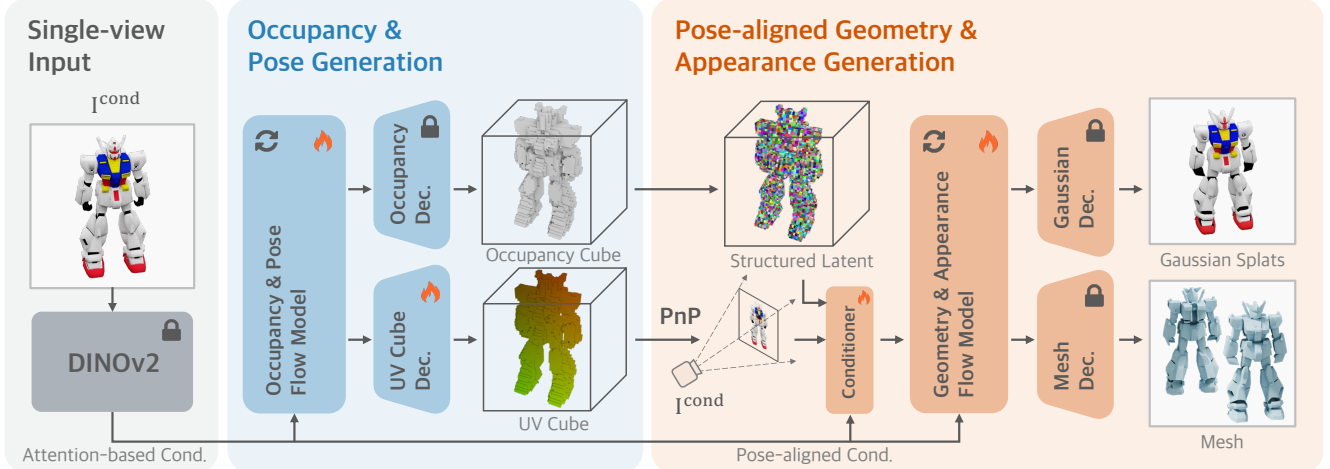


Figure 3. **Overview of CUPID’s pipeline.** From a single input image, CUPID first generates an occupancy and a UV cube in canonical space. Then, a *Perspective-n-Point (PnP)* solver (*i.e.*, Eq. 2) recovers the camera pose. Using this recovered camera pose, we extract pose-aligned conditioning latents and visual features (*i.e.*, Eq. 3), along with noisy structured latents, to generate the geometry and appearance features, which will be decoded to the 3D Gaussian splats and mesh.

stage pipeline for spatial alignment: it first estimates a point cloud [51] then aligns each generated object via 3D–3D correspondences. In contrast, our approach achieves image-to-3D alignment in a single forward pass while delivering monocular geometry quality on par with MoGe [51], enabling streamlined compositional scene reconstruction without complex pipelines.

3. Method

3.1. Problem definition and method overview

We formulate our generative reconstruction as estimating the joint posterior $p(\mathcal{O}, \theta \mid \mathbf{I}^{\text{cond}})$ under the observation constraint $\mathbf{I}^{\text{cond}} = \mathcal{P}(\mathcal{O}, \theta)$, where \mathbf{I}^{cond} is the input image, \mathcal{O} is the 3D object, θ is the object-centric camera pose, and $\mathcal{P}(\cdot, \cdot)$ projects the 3D object to the image.

We first use an encoder φ to map the 3D object and camera pose to a volumetric latent feature $\mathbf{z} = \varphi(\mathcal{O}, \theta)$, which can be decoded into 3D representations (e.g., Gaussian splats or meshes) by specific decoders [20, 41]. We use Rectified Flow [23] for the latent \mathbf{z} generation. The model interpolates between data \mathbf{z}_0 and noise ϵ over time t via $\mathbf{z}_t = (1 - t)\mathbf{z}_0 + t\epsilon$. The reverse process follows a time-dependent velocity field $\mathbf{v}(\mathbf{z}_t, \mathbf{I}^{\text{cond}}, t) = \nabla_t \mathbf{z}_t$ that drives noisy samples toward the data distribution. We parameterize \mathbf{v} with a neural network \mathbf{v}_ϕ and train it using the Conditional Flow Matching (CFM) objective:

$$\mathcal{L}_{\text{CFM}}(\phi) = \mathbb{E}_{t, \mathbf{z}_0, \epsilon} \|\mathbf{v}_\phi(\mathbf{z}_t, \mathbf{I}^{\text{cond}}, t) - (\epsilon - \mathbf{z}_0)\|_2^2. \quad (1)$$

We first describe the representation of objects and camera poses in Sec. 3.2. To enable efficient 3D generation, we utilize a cascaded flow modeling approach for \mathbf{v}_ϕ [59]. In the first stage, we generate an occupancy cube along with

the camera pose. The second stage predicts the 3D shape and texture features in the occupied regions based on the outputs from the first stage. This process is detailed in Sec. 3.3. The pipeline is illustrated in Fig. 3.

3.2. Representation of 3D Object and camera pose

3D object representation. To enable network training, we first tensorize 3D objects with a voxel-based representation: $\mathcal{O} \triangleq \{\mathbf{x}_i, \mathbf{f}_i\}_{i=1}^L$, where $\mathbf{x}_i \in \mathbb{R}^3$ represents the coordinates of the i -th active voxel in a cube, and \mathbf{f}_i encodes associated features derived from multi-view DINOv2 [32] feature aggregation, subsequently compressed by a 3D variational autoencoder (VAE) encoder. Here, L denotes the number of voxels. This voxel set can be decoded to 3D formats such as mesh or Gaussian splat [59].

Camera pose parameterization. Camera pose θ is represented by the projection matrix $\mathbf{P} = \mathbf{K}[\mathbf{R}|\mathbf{t}] \in \mathbb{R}^{3 \times 4}$, where \mathbf{K} is intrinsic, and (\mathbf{R}, \mathbf{t}) are extrinsic parameters mapping object to camera space. Inspired by recent pose estimation work [53, 69], we propose an over-parameterized pose representation[†] via an *in-cube pixel distribution*. Specifically, we reparameterize θ as dense 3D-2D correspondence: $\theta \triangleq \{\mathbf{x}_i, \mathbf{u}_i\}_{i=1}^L$ where $\mathbf{u}_i : (u_i, v_i) \in [0, 1]^2$ is the normalized 2D pixel coordinates anchored at the 3D voxel $\mathbf{x}_i \in \mathcal{O}$. Each anchor’s pixel coordinate is obtained by $\mathbf{u}_i = \pi(\mathbf{P}, \mathbf{x}_i)$, where π denotes perspective projection. Such a reparameterized pose, *i.e.*, 3D-2D correspondence, can be presented as a 3D UV cube. Given these correspondences, we recover the global camera matrix \mathbf{P}^*

[†]While camera pose can be encoded as a compact 1D token (e.g., a 12D vector), it can be challenging for 3D generators with 3D tokens [69].

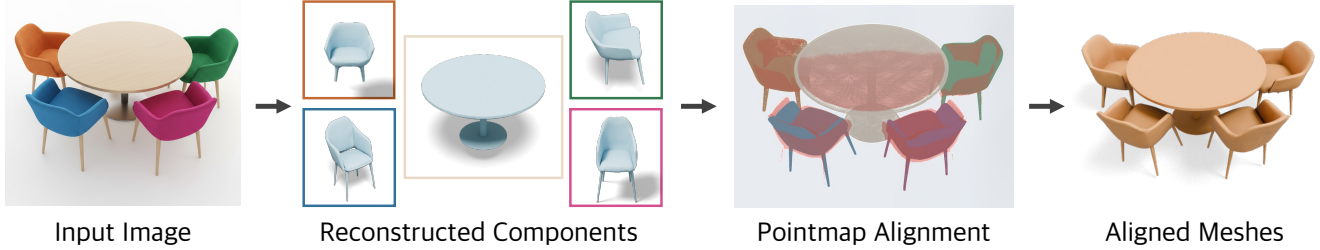


Figure 4. **Component-aligned scene reconstruction.** For a scene with multiple objects, our method can rebuild each object using the occlusion-aware 3D generator and then solve 3D–3D similarity transformation to accurately recompose the scene.

using a least-squares solver [1]:

$$\mathbf{P}^* = \arg \min_{\mathbf{P}} \sum_{i=1}^L \|\pi(\mathbf{P}, \mathbf{x}_i) - \mathbf{u}_i\|^2. \quad (2)$$

We then decompose \mathbf{P}^* into $(\mathbf{K}, \mathbf{R}, \mathbf{t})$ via RQ decomposition. Unlike image-based pose representations (e.g., 2D ray or point maps [53, 69]), we reparameterize pose within a 3D cube. Intuitively, the (u, v) coordinates act like view-dependent colors defined on a 3D occupancy grid (see the UV cube in the Fig. 3). Under this view, joint object–pose generation transforms to producing a 3D object with view-dependent colors.

3.3. Cascaded Flow Modeling

We employ a two-stage cascaded flow model to jointly sample a 3D object and its corresponding camera pose, *i.e.*, $\mathbf{z} = \{(\mathbf{x}_i, \mathbf{f}_i), (\mathbf{x}_i, \mathbf{u}_i)\}_{i=1}^L$. In the first stage, the flow model for occupancy and pose generation (\mathcal{G}_S) generates (i) an occupancy cube that indicates active voxels and (ii) a UV cube that encodes object-centric camera pose (Sec. 3.2). In the second stage, conditioned on the predicted occupancy and camera pose, the pose-aligned geometry and appearance generation model \mathcal{G}_L synthesizes DINO features \mathbf{f}_i for each active voxel, yielding the final \mathbf{z} .

Occupancy and pose generation. In this stage, given a conditioning image \mathbf{I}^{cond} , we generate an occupancy cube and a UV cube with resolution r . The occupancy cube $\mathbf{G}_o \in \{0, 1\}^{r \times r \times r \times 1}$ encodes binary values indicating active/inactive voxels. The UV cube $\mathbf{G}_{uv} \in [0, 1]^{r \times r \times r \times 2}$ stores normalized pixel coordinates (u, v) for each voxel. Voxels sharing the same pixel coordinates lie on the same ray[‡]. Next, we train a 3D VAE to compress the UV cube into a low-resolution feature grid $\mathbf{S}_{uv} \in \mathbb{R}^{s \times s \times s \times C}$, improving efficiency with near-lossless pose accuracy (mean RRE / RTE $< 0.5^\circ$). For fine-tuning TRELLIS, we concatenate the original feature grid \mathbf{S}_o with \mathbf{S}_{uv} and incorporate linear layers at both the input and output of the flow

[‡]We do not model occlusion as recent studies suggest that transformers can effectively model light transport [18, 68].

network \mathcal{G}_S . Once the occupancy and UV cubes are generated, we obtain $\{(\mathbf{x}_i, \mathbf{u}_i(\boldsymbol{\theta}))\}_{i=1}^L$ by collecting active voxels and solving the camera pose with Eq. 2.

Pose-aligned geometry and appearance generation. In this stage, we generate the detailed 3D latent $\{\mathbf{f}_i\}_{i=1}^L$ only at active voxels. Our experiments show that the original \mathcal{G}_L from TRELLIS, which uses globally-attended image information, often suffers from color drift and loss of fine details (see Fig. 9 in App. A.4). To address this, we leverage the calculated camera pose from the first stage to inject locally attended pixel information in each voxel.

Specifically, we leverage the estimated camera pose to compute the features located at the i -th voxel as follows:

$$\begin{aligned} \mathbf{f}_i^{\text{DINO}} &= \text{BilinearInterp}(\mathbf{u}_i, \text{DINO}(\mathbf{I}^{\text{cond}})) \in \mathbb{R}^{1024}, \\ \{\mathbf{f}_i^h\}_{i=1}^L &= \text{SlatEncoder}(\{\mathbf{x}_i, \mathbf{f}_i^{\text{DINO}}\}_{i=1}^L), \quad \mathbf{f}_i^h \in \mathbb{R}^8, \end{aligned} \quad (3)$$

where each voxel’s pixel coordinate \mathbf{u}_i is obtained by projecting the coordinates of the i -th 3D voxel center onto the image plane with the calculated camera pose, BilinearInterp denotes bilinear interpolation and SlatEncoder is the 3D VAE encoder. While DINO captures high-level semantics, it loses low-level cues needed for precise 3D geometry and appearance reconstruction. To compensate, we extract complementary low-level features \mathbf{f}^l from \mathbf{I}^{cond} with a lightweight convolutional head and sample them at \mathbf{u}_i via BilinearInterp . Finally, for each voxel, we concatenate the current noisy voxel feature \mathbf{f}_i^t at time step t with the pixel-aligned features and fuse them into the flow transformer with a linear layer: $l_t = \text{Linear}([\mathbf{f}_i^t \oplus \mathbf{f}_i^h \oplus \mathbf{f}_i^l])$. This pose-aligned fusion significantly improves 3D geometry accuracy and appearance fidelity with respect to the input image.

4. Component-aligned Scene Reconstruction

By explicitly modeling the spatial relationship between the generated object and the input camera pose, our approach seamlessly integrates powerful generative priors into 3D reconstruction. CUPID naturally extends to scene-level compositional reconstruction by using explicit 3D-to-2D corre-

Table 1. **Monocular geometry accuracy.** CUPID outperforms all 3D reconstruction and generation baselines and matches point-map regression methods that predict only partial geometry. Note that VGGT uses a ground-truth object mask, which may overestimate accuracy.

Method	3D	Toys4k					GSO				
		mIOU (avg)↑	CD (avg)↓	CD (med)↓	F-score (0.01)↑	F-score (0.05)↑	mIOU (avg)↑	CD (avg)↓	CD (med)↓	F-score (0.01)↑	F-score (0.05)↑
VGGT	×	–	1.144	0.498	61.85	95.90	–	1.396	0.388	65.98	95.95
MoGe	×	92.80	1.284	0.581	58.54	95.31	96.18	1.743	0.575	58.99	94.68
OnePoseGen	✓	9.34	153.2	59.92	6.11	24.10	12.16	116.2	60.56	7.28	25.77
LaRa	✓	68.11	32.15	16.59	18.57	57.67	70.63	34.23	19.36	13.48	49.95
OpenLRM	✓	86.26	2.726	1.291	40.42	90.60	91.35	3.741	1.858	34.14	87.20
Ours	✓	92.43	2.534	0.236	69.82	97.76	95.27	1.823	0.434	61.01	95.59



Figure 5. **Qualitative comparison on input view consistency.** We render the input view using its generated camera pose. For view centric methods (LRM, LaRa), we use ground-truth intrinsic for rendering as they do not model intrinsic. Our method produces the highest-fidelity geometry and appearance; LRM hallucinates incorrect details, LaRa is overly blurry due to 2D diffusion inconsistencies, and 3D generation method OnePoseGen frequently fails to register pose reliably.

spondences for spatial alignment. We first harness foundation models for object segmentation [35], generate each 3D object, and compose them into a scene with a global depth prior [52]. Fig. 4 shows one such result with our method. More results are given in Fig. 10 of App. A.3.

Occlusion-aware 3D generation. Images with multiple objects often contain mutual occlusions, which our synthetic training data do not model. To address this, we introduce random masks on the conditioning image during fine-tuning, inspired by Amodal3R [58]. We adapt their masking strategy to our architecture; see App. A.2 for implementation. Then, given an input image with multiple objects and their corresponding object masks, we reconstruct each object independently with our occlusion-aware generator, yielding dense 3D–2D correspondences per object.

Multi-component composition. Since absolute depth is not preserved across objects, direct 3D–2D alignment to the image is ill-posed. We address this using MoGe [51] to predict a global pointmap, thereby reducing 3D–2D alignment to 3D–3D alignment. For the k -th object, we collect the matched pair $(\mathbf{x}_i^k, \mathbf{u}_i)$, where \mathbf{x}_i^k is the coordinates of a visible 3D point on the generated 3D object and \mathbf{u}_i is the corresponding pixel coordinates within the mask M^k . We query the MoGe pointmap to obtain $\mathbf{p}_i = P(\mathbf{u}_i)$ in the camera frame, then estimate a per-object similarity transformation $\mathcal{S}_k = (s_k, \mathbf{R}_k, \mathbf{t}_k)$ via the Umeyama method [47] on pairs $(\mathbf{x}_i^k, \mathbf{p}_i)$. Applying \mathcal{S}_k places each object in the shared camera frame, yielding a component-aligned scene reconstruction. This composition can also extend to multi-view input using VGGT [48], allowing for more flexible input and transforming partial geometry into holistic geometry.

Table 2. **Input-view consistency.** CUPID achieves superior input view consistency, producing accurate appearance alignment.

Dataset Method	Pose	Toys4K			GSO		
		PSNR \uparrow	SSIM \uparrow	LPIPS \downarrow	PSNR \uparrow	SSIM \uparrow	LPIPS \downarrow
LaRa	×	22.00	93.42	0.0884	19.81	91.61	0.1119
OpenLRM	×	26.41	80.17	0.1156	25.79	78.80	0.1268
OnePoseGen	✓	17.43	89.37	0.1174	14.87	86.46	0.1386
Ours	✓	30.05	96.81	0.0251	28.68	95.49	0.0354

Table 3. **Comparison on full 3D quality.** We report CLIP image scores of novel views following [11].

	OnePoseGen	LaRa	OpenLRM	TRELLIS	Ours
ViT-B/16	0.7933	0.8334	0.8939	0.9465	0.9501
ViT-L/14	0.7193	0.7682	0.8410	0.9210	0.9291

5. Experiments

We evaluate key baselines on three tasks: monocular geometry prediction, input-view consistency, and single-image-to-3D reconstruction in Sec. 5.1. We exclude per-scene optimization methods and focus on learning-based systems. We ablate pose-conditioning in Sec. 5.2, with implementation details and pose encoding accuracy in App. A.1. We do not extensively compare with state-of-the-art 3D generators, as improving their aesthetic or geometric quality is orthogonal to our goal. Qualitative comparisons with our baseline [59] for input-view consistency appear in Sec. A.4.

5.1. Evaluation

Baselines. We compare against three complementary families for single image 3D reconstruction: point-map regression, view-centric 3D reconstruction, and 3D generation with post-hoc pose alignment.

Point-map regression. VGGT [48] and MoGe [51] simultaneously predict per-pixel 3D points and view-centric camera pose for 2D-to-3D reconstruction. These methods reconstruct only the geometry visible in the input view, often lacking robust priors for occluded regions. *View-centric 3D reconstruction.* LRM [16] and LaRa [4] generate view-centric 3D models, eliminating the need to estimate camera parameters at test time. LRM directly regresses 3D objects in view space, while LaRa enhances the input with novel views from Zero123++ [42] before reconstruction. We adopt an open-source implementation of LRM [13] for comparisons. *3D generation with post-hoc alignment.* OnePoseGen [12] integrates Higen3D [66] and TRELLIS [59], which produces canonical 3D models, with FoundationPose [56] to align the 3D model with the input view. This approach evaluates whether decoupling 3D generation from pose estimation and applying post-hoc alignment can achieve reprojection consistency.

Evaluation. We evaluate three aspects: (i) monocular geometry accuracy, (ii) input-view consistency to assess reprojection alignment and appearance fidelity, and (iii) novel-view consistency to assess full 3D fidelity. Experi-

Table 4. **Ablation studies of pose-aligned conditioning.**

Method	GT Geo & Pose			Sampled Geo & Pose		
	PSNR	SSIM	LPIPS	PSNR	SSIM	LPIPS
(a) Baseline (w/o PAC)	31.84	97.50	0.0219	27.47	95.64	0.0327
(b) Position Embedding	32.07	97.58	0.0211	27.56	95.67	0.0323
(c) Latent (w/o Occ.)	32.37	97.72	0.0201	27.85	95.87	0.0309
(d) Latent (Occ.)	32.39	97.77	0.0199	27.74	95.80	0.0313
(e) Latent (Visual Feat.)	34.86	98.24	0.0168	30.05	96.81	0.0251

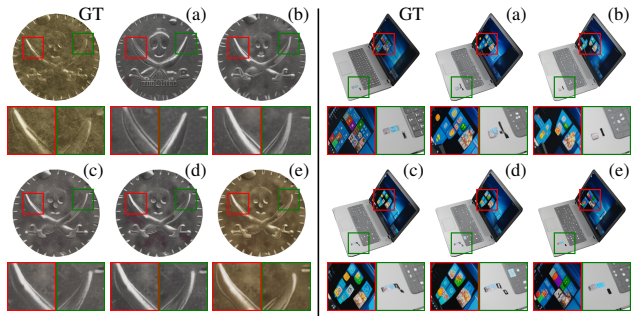


Figure 6. **Qualitative comparison of various pose-aligned conditioning.** Our method (e) achieves the best visual quality in terms of color fidelity and detail.

ments are conducted on Toys4K [44] and GSO [9], containing approximately 3K synthetic and 1K real-world objects, respectively. For novel views, we render four uniform views rotating around the vertical axis. Tasks (i) and (ii) are particularly challenging for generative approaches, as they require producing accurate an object-centric camera pose that aligns with the input view.

Monocular geometry accuracy. Monocular geometry metrics evaluate pose alignment and visible geometry fidelity. Unlike multi-view approaches that report pose accuracy relative to the first frame, single-view generation cannot report relative pose metrics. Following MoGe [51], we use monocular geometry alignment as a proxy for pose accuracy. We construct ground-truth (GT) point clouds by unprojecting depth maps with camera parameters and report Mask IoU, Chamfer Distance (CD), and F-score, providing both mean and median statistics to mitigate outlier sensitivity. Since VGGT outputs point maps without masks, we use GT masks to avoid background contamination. For full 3D methods, we render and unproject the depth map to obtain the visible point cloud, using rendered alphas as the mask. Predicted point clouds are aligned to GT using scale-shift alignment from MoGe [51]. Results are in Tab. 1.

Our approach demonstrates clear superiority over view-centric reconstruction methods such as LRM and LaRa. On the GSO dataset, it reduces the average Chamfer Distance (CD) by 50% relative to LRM. This improvement stems not only from accurate intrinsic modeling via generative priors but also from our precise extrinsic camera parameter prediction. By contrast, although OnePoseGen excels in intrinsic modeling, it falls short on Toys4K and GSO, as



Figure 7. **Multi-view conditioning.** Our decoupled joint modeling naturally supports multi-view conditioning. When multiple input views are available, we fuse the shared *view-agnostic* object latent across flow paths (similar to MultiDiffusion [2]), enabling object and cameras refinement across all views. Top: inputs; Middle: reconstructed 3D object and camera poses; Bottom: rendered images and geometry.

these datasets contain geometric symmetries and texture-less regions that cause its registration modules to fail during extrinsic pose estimation. Crucially, our model is also highly competitive with methods that produce only partial geometries (e.g., VGGT, MoGe). This suggests that complex, multi-stage pipelines which use these partial methods as a first step [65] can be streamlined. Our approach achieves comparable monocular accuracy in a single step, eliminating the need for such intermediate representations.

Input view consistency. We evaluate input view consistency to measure alignment between the 3D reconstruction and the input image. We quantify the difference between the re-rendered and input images, reporting PSNR, SSIM, and LPIPS in Tab. 2, with qualitative comparisons in Fig. 5. Our method achieves substantial fidelity improvements over existing reconstruction-based methods. We find LaRa’s texture quality is affected by inconsistencies in the generated novel views, while LRM struggles to predict detailed textures. OnePoseGen can produce plausible 3D objects but suffers severely from texture misalignment (e.g., color shifting), often failing on pose estimation. Our method achieves strong pose accuracy while retaining high-quality texture details, as evidenced by the zoomed-in views in Fig. 5.

Full 3D evaluation. Evaluating single-image-to-3D is challenging because many distinct 3D shapes can explain a single view. We therefore emphasize (1) qualitative assessments (Fig. 5) and (2) quantitative semantic alignment using CLIP similarity [34] on Toys4K (Tab. 3). Our method consistently outperforms all baselines. Moreover, it reconstructs high-fidelity 3D objects and scenes from in-the-wild images (Fig. 2), which prior methods do not achieve.

5.2. Ablation Studies

We compare pose-aligned conditioning (PAC) variants in the second-stage refinement on Toys4K: (a) the TRELIS baseline (without PAC); (b) adding DINOv2 positional embeddings to SLat latents; (c) concatenating DINOv2 fea-

ture volumes with view-conditioned voxel latents from the frozen SLat encoder; (d) as in (c) but zeroing latents of occluded voxels in the input view; and (e) concatenating additional visual features from a convolutional layer applied to the input image. We report results using both GT coarse geometry and camera pose, and samples from the first stage.

As shown in Tab. 4, when provided with ground-truth coarse geometry and camera pose, methods (b) and (c) validate the benefit of pose-aligned conditioning in generating geometry and appearance; (d) indicates that performance remains consistent whether occlusion is present or absent; our full method (e) provides the best visual quality by supplementing DINOv2 features with missing low-level cues, yielding better color and detail alignment, as shown in Fig. 6. Crucially, these advantages are largely preserved when using sampled geometry and camera poses from the first stage (30.05 PSNR for (e) vs. 27.47 for baseline (a)). This confirms that our pose-aligned conditioning is highly robust to small perturbations from stochastic generation.

6. Discussion

We present CUPID, a *generative reconstruction* framework that unifies 3D generation and reconstruction by jointly modeling canonical 3D object and camera pose that formulate a given observation. By incorporating the missing camera pose prior and pose-aligned conditioning into 3D generators, this simple yet effective design enables CUPID to significantly improve geometric and photometric consistency with the input image for single-view reconstruction.

Despite strong performance and consistent gains over prior methods, CUPID has limitations. First, it requires object masks like existing 3D generation methods, and boundary errors in real images can degrade reconstruction quality. Second, lighting can be baked into the appearance, which can be improved with better material–light disentanglement. Third, our synthetic training images are mostly centered, making off-centered objects more challenging in real scenes. Nevertheless, these are not fundamental limitations and can be alleviated with better data and supervision.

Looking forward, this generative reconstruction framework enables promising test-time extensions, particularly for *multi-view* scenarios. From multiple images, our method refines 3D reconstructions to align with all observations by fusing a shared object latent during sampling, similar to Multi-Diffusion [2]. As shown in Fig. 7, this yields an SfM-like system, though challenges like misaligned 3D orientations [31] from diverse views require advanced fusion schemes. Moreover, CUPID’s joint modeling enables bidirectional capabilities: flexible generation with known poses or pose estimation from images of given objects, facilitating mixed reality and embodied AI applications.

References

- [1] Yousset I Abdel-Aziz, Hauck Michael Karara, and Michael Hauck. Direct linear transformation from comparator coordinates into object space coordinates in close-range photogrammetry. *Photogrammetric engineering & remote sensing*, 81(2):103–107, 2015. 3, 5
- [2] Omer Bar-Tal, Lior Yariv, Yaron Lipman, and Tali Dekel. Multidiffusion: Fusing diffusion paths for controlled image generation. In *International Conference on Machine Learning*, pages 1737–1752. PMLR, 2023. 8, 9
- [3] Yohann Cabon, Lucas Stofl, Leonid Antsfeld, Gabriela Csurka, Boris Chidlovskii, Jerome Revaud, and Vincent Leroy. Must3r: Multi-view network for stereo 3d reconstruction. In *CVPR*, 2025. 3
- [4] Anpei Chen, Haofei Xu, Stefano Esposito, Siyu Tang, and Andreas Geiger. Lara: Efficient large-baseline radiance fields. In *European Conference on Computer Vision (ECCV)*, 2024. 3, 7
- [5] Hansheng Chen, Pichao Wang, Fan Wang, Wei Tian, Lu Xiong, and Hao Li. Epro-pnp: Generalized end-to-end probabilistic perspective-n-points for monocular object pose estimation. In *Proceedings of the IEEE/CVF conference on computer vision and pattern recognition*, pages 2781–2790, 2022. 3
- [6] Jasmine Collins, Shubham Goel, Kenan Deng, Achleshwar Luthra, Leon Xu, Erhan Gundogdu, Xi Zhang, Tomas F Yago Vicente, Thomas Dideriksen, Himanshu Arora, et al. Abo: Dataset and benchmarks for real-world 3d object understanding. In *Proceedings of the IEEE/CVF conference on computer vision and pattern recognition*, pages 21126–21136, 2022. 13
- [7] Matt Deitke, Ruoshi Liu, Matthew Wallingford, Huong Ngo, Oscar Michel, Aditya Kusupati, Alan Fan, Christian Laforte, Vikram Voleti, Samir Yitzhak Gadre, et al. Objaverse-xl: A universe of 10m+ 3d objects. *Advances in Neural Information Processing Systems*, 36:35799–35813, 2023. 13
- [8] Wenqi Dong, Bangbang Yang, Zesong Yang, Yuan Li, Tao Hu, Hujun Bao, Yuwen Ma, and Zhaopeng Cui. Hiscene: creating hierarchical 3d scenes with isometric view generation. *arXiv preprint arXiv:2504.13072*, 2025. 1, 3
- [9] Laura Downs, Anthony Francis, Nate Koenig, Brandon Kinman, Ryan Hickman, Krista Reymann, Thomas B McHugh, and Vincent Vanhoucke. Google scanned objects: A high-quality dataset of 3d scanned household items. In *2022 International Conference on Robotics and Automation (ICRA)*, pages 2553–2560. IEEE, 2022. 7
- [10] Huan Fu, Rongfei Jia, Lin Gao, Mingming Gong, Binqiang Zhao, Steve Maybank, and Dacheng Tao. 3d-future: 3d furniture shape with texture. *International Journal of Computer Vision*, 129(12):3313–3337, 2021. 13
- [11] Ruiqi Gao, Aleksander Holy’nski, Philipp Henzler, Arthur Brussee, Ricardo Martin-Brualla, Pratul Srinivasan, Jonathan T. Barron, and Ben Poole. Cat3d: Create anything in 3d with multi-view diffusion models. In *Advances in Neural Information Processing Systems (NeurIPS)*, 2024. Oral. 3, 7
- [12] Zheng Geng, Nan Wang, Shaocong Xu, Chongjie Ye, Bohan Li, Zhaoxi Chen, Sida Peng, and Hao Zhao. One view, many worlds: Single-image to 3d object meets generative domain randomization for one-shot 6d pose estimation. *arXiv preprint arXiv:2509.07978*, 2025. 1, 7
- [13] Zexin He and Tengfei Wang. Openlrm: Open-source large reconstruction models. <https://github.com/3DTopia/OpenLRM>, 2023. 7
- [14] Jonathan Ho and Tim Salimans. Classifier-free diffusion guidance. *arXiv preprint arXiv:2207.12598*, 2022. 13
- [15] Lukas Höllein, Aljaž Božič, Norman Müller, David Novotny, Hung-Yu Tseng, Christian Richardt, Michael Zollhöfer, and Matthias Nießner. Viewdiff: 3d-consistent image generation with text-to-image models. In *Proceedings of the IEEE/CVF Conference on Computer Vision and Pattern Recognition*, 2024. 3
- [16] Yicong Hong, Kai Zhang, Jiuxiang Gu, Sai Bi, Yang Zhou, Difan Liu, Feng Liu, Kalyan Sunkavalli, Trung Bui, and Hao Tan. Lrm: Large reconstruction model for single image to 3d. *arXiv preprint arXiv:2311.04400*, 2023. 1, 3, 7, 14
- [17] Zehuan Huang, Yuan-Chen Guo, Xingqiao An, Yunhan Yang, Yanguang Li, Zi-Xin Zou, Ding Liang, Xihui Liu, Yan-Pei Cao, and Lu Sheng. Midi: Multi-instance diffusion for single image to 3d scene generation. In *Proceedings of the Computer Vision and Pattern Recognition Conference*, pages 23646–23657, 2025. 3
- [18] Haian Jin, Hanwen Jiang, Hao Tan, Kai Zhang, Sai Bi, Tianyuan Zhang, Fujun Luan, Noah Snavely, and Zexiang Xu. Lvsm: A large view synthesis model with minimal 3d inductive bias. *arXiv preprint arXiv:2410.17242*, 2024. 5
- [19] Nikita Karaev, Iurii Makarov, Jianyuan Wang, Natalia Neverova, Andrea Vedaldi, and Christian Rupprecht. Co-tracker3: Simpler and better point tracking by pseudo-labelling real videos. In *Proc. arXiv:2410.11831*, 2024. 3
- [20] Bernhard Kerbl, Georgios Kopanas, Thomas Leimkühler, and George Drettakis. 3d gaussian splatting for real-time radiance field rendering. *ACM Trans. Graph.*, 42(4):139–1, 2023. 4
- [21] Mukul Khanna, Yongsan Mao, Hanxiao Jiang, Sanjay Haresh, Brennan Shacklett, Dhruv Batra, Alexander Clegg, Eric Undersander, Angel X Chang, and Manolis Savva. Habitat synthetic scenes dataset (hssd-200): An analysis of 3d scene scale and realism tradeoffs for objectgoal naviga-

- tion. In *Proceedings of the IEEE/CVF Conference on Computer Vision and Pattern Recognition*, pages 16384–16393, 2024. 13
- [22] Jiahao Li, Hao Tan, Kai Zhang, Zexiang Xu, Fujun Luan, Yinghao Xu, Yicong Hong, Kalyan Sunkavalli, Greg Shakhnarovich, and Sai Bi. Instant3d: Fast text-to-3d with sparse-view generation and large reconstruction model. In *Proceedings of the International Conference on Learning Representations (ICLR)*, 2024. 3
- [23] Yaron Lipman, Ricky TQ Chen, Heli Ben-Hamu, Maximilian Nickel, and Matt Le. Flow matching for generative modeling. *arXiv preprint arXiv:2210.02747*, 2022. 4
- [24] Jiayi Liu, Hou In Ivan Tam, Ali Mahdavi-Amiri, and Manolis Savva. Cage: Controllable articulation generation. In *Proceedings of the IEEE/CVF Conference on Computer Vision and Pattern Recognition*, pages 17880–17889, 2024. 1
- [25] Minghua Liu, Chao Xu, Haian Jin, Linghao Chen, Mukund Varma T, Zexiang Xu, and Hao Su. One-2-3-45: Any single image to 3d mesh in 45 seconds without per-shape optimization. *Advances in Neural Information Processing Systems*, 36, 2023. 3
- [26] Minghua Liu, Chong Zeng, Xinyue Wei, Ruoxi Shi, Linghao Chen, Chao Xu, Mengqi Zhang, Zhaoning Wang, Xiaoshuai Zhang, Isabella Liu, Hongzhi Wu, and Hao Su. Meshformer: High-quality mesh generation with 3d-guided reconstruction model. *arXiv preprint arXiv:2408.10198*, 2024. 3
- [27] Ruoshi Liu, Rundi Wu, Basile Van Hoorick, Pavel Tokmakov, Sergey Zakharov, and Carl Vondrick. Zero-1-to-3: Zero-shot one image to 3d object, 2023. 3
- [28] Yuzheng Liu, Siyan Dong, Shuzhe Wang, Yingda Yin, Yanchao Yang, Qingnan Fan, and Baoquan Chen. Slam3r: Real-time dense scene reconstruction from monocular rgb videos. *arXiv preprint arXiv:2412.09401*, 2024. 3
- [29] Yuan Liu, Cheng Lin, Zijiao Zeng, Xiaoxiao Long, Lingjie Liu, Taku Komura, and Wenping Wang. Syncdreamer: Generating multiview-consistent images from a single-view image. In *Proceedings of the International Conference on Learning Representations (ICLR)*, 2024. 3
- [30] Ilya Loshchilov and Frank Hutter. Decoupled weight decay regularization. *arXiv preprint arXiv:1711.05101*, 2017. 13
- [31] Yichong Lu, Yuzhuo Tian, Zijin Jiang, Yikun Zhao, Yuanbo Yang, Hao Ouyang, Haoji Hu, Huimin Yu, Yujun Shen, and Yiyi Liao. Orientation matters: Making 3d generative models orientation-aligned. *arXiv preprint arXiv:2506.08640*, 2025. 1, 9
- [32] Maxime Oquab, Timothée Darcet, Theo Moutakanni, Huy V. Vo, Marc Szafraniec, Vasil Khalidov, Pierre Fernandez, Daniel Haziza, Francisco Massa, Alaaeldin El-Nouby, Russell Howes, Po-Yao Huang, Hu Xu, Vasu Sharma, Shangwen Li, Wojciech Galuba, Mike Rabbat, Mido Assran, Nicolas Ballas, Gabriel Synnaeve, Ishan Misra, Herve Jegou, Julien Mairal, Patrick Labatut, Armand Joulin, and Piotr Bojanowski. DINOv2: Learning robust visual features without supervision, 2023. 4
- [33] Ben Poole, Ajay Jain, Jonathan T Barron, and Ben Mildenhall. Dreamfusion: Text-to-3d using 2d diffusion. *arXiv preprint arXiv:2209.14988*, 2022. 3
- [34] Alec Radford, Jong Wook Kim, Chris Hallacy, Aditya Ramesh, Gabriel Goh, Sandhini Agarwal, Girish Sastry, Amanda Askell, Pamela Mishkin, Jack Clark, et al. Learning transferable visual models from natural language supervision. In *International conference on machine learning*, pages 8748–8763. Pmlr, 2021. 8
- [35] Nikhila Ravi, Valentin Gabeur, Yuan-Ting Hu, Ronghang Hu, Chaitanya Ryali, Tengyu Ma, Haitham Khedr, Roman Rädle, Chloe Rolland, Laura Gustafson, et al. Sam 2: Segment anything in images and videos. *arXiv preprint arXiv:2408.00714*, 2024. 6
- [36] Xuanchi Ren, Tianchang Shen, Jiahui Huang, Huan Ling, Yifan Lu, Merlin Nimier-David, Thomas Müller, Alexander Keller, Sanja Fidler, and Jun Gao. Gen3c: 3d-informed world-consistent video generation with precise camera control. In *Proceedings of the IEEE/CVF Conference on Computer Vision and Pattern Recognition*, 2025. 3
- [37] Robin Rombach, Andreas Blattmann, Dominik Lorenz, Patrick Esser, and Björn Ommer. High-resolution image synthesis with latent diffusion models, 2021. 3
- [38] Chitwan Saharia, William Chan, Saurabh Saxena, Lala Li, Jay Whang, Emily Denton, Seyed Kamyar Seyed Ghasemipour, Burcu Karagol Ayan, S. Sara Mahdavi, Rapha Gontijo Lopes, Tim Salimans, Jonathan Ho, David J Fleet, and Mohammad Norouzi. Photorealistic text-to-image diffusion models with deep language understanding. In *Advances in Neural Information Processing Systems (NeurIPS)*, 2022. 3
- [39] Johannes Lutz Schönberger and Jan-Michael Frahm. Structure-from-motion revisited. In *Conference on Computer Vision and Pattern Recognition (CVPR)*, 2016. 1, 3
- [40] Johannes Lutz Schönberger, Enliang Zheng, Marc Pollefeys, and Jan-Michael Frahm. Pixelwise view selection for unstructured multi-view stereo. In *European Conference on Computer Vision (ECCV)*, 2016. 3
- [41] Tianchang Shen, Jacob Munkberg, Jon Hasselgren, Kangxue Yin, Zian Wang, Wenzheng Chen, Zan Gojcic, Sanja Fidler, Nicholas Sharp, and Jun Gao. Flexible isosurface extraction for gradient-based mesh optimization. *ACM Transactions on Graphics (TOG)*, 42(4):1–16, 2023. 4
- [42] Ruoxi Shi, Hansheng Chen, Zhuoyang Zhang, Minghua Liu, Chao Xu, Xinyue Wei, Linghao Chen, Chong Zeng, and Hao Su. Zero123++: a single image to consistent multi-view diffusion base model. *arXiv preprint arXiv:2310.15110*, 2023. 3, 7
- [43] Kiwhan Song, Boyuan Chen, Max Simchowitz, Yilun Du, Russ Tedrake, and Vincent Sitzmann. History-guided video diffusion, 2025. 3
- [44] Stefan Stojanov, Anh Thai, and James M Rehg. Using shape to categorize: Low-shot learning with an explicit shape bias. In *Proceedings of the IEEE/CVF conference on computer vision and pattern recognition*, pages 1798–1808, 2021. 7
- [45] Jiaxiang Tang, Zhaoxi Chen, Xiaokang Chen, Tengfei Wang, Gang Zeng, and Ziwei Liu. Lgm: Large multi-view gaussian model for high-resolution 3d content creation. *arXiv preprint arXiv:2402.05054*, 2024. 3
- [46] Dmitry Tochilkin, David Pankratz, Zexiang Liu, Zixuan Huang, Adam Letts, Yangguang Li, Ding Liang, Christian

- Laforte, Varun Jampani, and Yan-Pei Cao. Tripopr: Fast 3d object reconstruction from a single image. *arXiv preprint arXiv:2403.02151*, 2024. 3
- [47] Shinji Umeyama. Least-squares estimation of transformation parameters between two point patterns. *IEEE Transactions on pattern analysis and machine intelligence*, 13(4): 376–380, 2002. 6
- [48] Jianyuan Wang, Minghao Chen, Nikita Karaev, Andrea Vedaldi, Christian Rupprecht, and David Novotny. Vggt: Visual geometry grounded transformer. In *Proceedings of the Computer Vision and Pattern Recognition Conference*, pages 5294–5306, 2025. 1, 3, 6, 7
- [49] Peng Wang, Hao Tan, Sai Bi, Yinghao Xu, Fujun Luan, Kalyan Sunkavalli, Wenping Wang, Zexiang Xu, and Kai Zhang. Pf-lrm: Pose-free large reconstruction model for joint pose and shape prediction. *arXiv preprint arXiv:2311.12024*, 2023. 1, 3
- [50] Qianqian Wang, Yifei Zhang, Aleksander Holynski, Alexei A. Efros, and Angjoo Kanazawa. Continuous 3d perception model with persistent state. In *Proceedings of the IEEE/CVF Conference on Computer Vision and Pattern Recognition (CVPR)*, pages 10510–10522, 2025. 3
- [51] Ruicheng Wang, Sicheng Xu, Cassie Dai, Jianfeng Xiang, Yu Deng, Xin Tong, and Jiaolong Yang. Moge: Unlocking accurate monocular geometry estimation for open-domain images with optimal training supervision. In *Proceedings of the Computer Vision and Pattern Recognition Conference*, pages 5261–5271, 2025. 1, 3, 4, 6, 7
- [52] Ruicheng Wang, Sicheng Xu, Yue Dong, Yu Deng, Jianfeng Xiang, Zelong Lv, Guangzhong Sun, Xin Tong, and Jiaolong Yang. Moge-2: Accurate monocular geometry with metric scale and sharp details, 2025. 3, 6
- [53] Shuzhe Wang, Vincent Leroy, Yohann Cabon, Boris Chidlovskii, and Jerome Revaud. Dust3r: Geometric 3d vision made easy. In *Proceedings of the IEEE/CVF Conference on Computer Vision and Pattern Recognition*, pages 20697–20709, 2024. 1, 3, 4, 5
- [54] Daniel Watson, William Chan, Ricardo Martin-Brualla, Jonathan Ho, Andrea Tagliasacchi, and Mohammad Norouzi. Novel view synthesis with diffusion models. *arXiv preprint arXiv:2210.04628*, 2022. 3
- [55] Xinyue Wei, Kai Zhang, Sai Bi, Hao Tan, Fujun Luan, and Valentin Deschaintre. Meshlrm: Large reconstruction model for high-quality meshes. *arXiv preprint*, 2024. 3
- [56] Bowen Wen, Wei Yang, Jan Kautz, and Stan Birchfield. Foundationpose: Unified 6d pose estimation and tracking of novel objects. In *Proceedings of the IEEE/CVF Conference on Computer Vision and Pattern Recognition*, pages 17868–17879, 2024. 7
- [57] Rundi Wu, Ben Mildenhall, Philipp Henzler, Keunhong Park, Ruiqi Gao, Daniel Watson, Pratul P. Srinivasan, Dor Verbin, Jonathan T. Barron, Ben Poole, and Aleksander Holyński. Reconfusion: 3d reconstruction with diffusion priors. In *Proceedings of the IEEE/CVF Conference on Computer Vision and Pattern Recognition (CVPR)*, 2024. 3
- [58] Tianhao Wu, Chuanxia Zheng, Frank Guan, Andrea Vedaldi, and Tat-Jen Cham. Amodal3r: Amodal 3d reconstruction from occluded 2d images. *arXiv preprint arXiv:2503.13439*, 2025. 6, 13
- [59] Jianfeng Xiang, Zelong Lv, Sicheng Xu, Yu Deng, Ruicheng Wang, Bowen Zhang, Dong Chen, Xin Tong, and Jiaolong Yang. Structured 3d latents for scalable and versatile 3d generation. In *Proceedings of the Computer Vision and Pattern Recognition Conference*, pages 21469–21480, 2025. 1, 3, 4, 7, 13, 14, 15
- [60] Chao Xu, Ang Li, Linghao Chen, Yulin Liu, Ruoxi Shi, Hao Su, and Minghua Liu. Sparp: Fast 3d object reconstruction and pose estimation from sparse views. In *European Conference on Computer Vision*, pages 143–163. Springer, 2024. 3
- [61] Jiale Xu, Weihao Cheng, Yiming Gao, Xintao Wang, Shenghua Gao, and Ying Shan. Instantmesh: Efficient 3d mesh generation from a single image with sparse-view large reconstruction models. *arXiv preprint arXiv:2404.07191*, 2024. 3
- [62] Jiale Xu, Shenghua Gao, and Ying Shan. Freesplatter: Pose-free gaussian splatting for sparse-view 3d reconstruction. *arXiv preprint arXiv:2412.09573*, 2024. 3
- [63] Jianing Yang, Alexander Sax, Kevin J. Liang, Mikael Henaff, Hao Tang, Ang Cao, Joyce Chai, Franziska Meier, and Matt Feiszli. Fast3r: Towards 3d reconstruction of 1000+ images in one forward pass. In *Proceedings of the IEEE/CVF Conference on Computer Vision and Pattern Recognition (CVPR)*, 2025. 3
- [64] Lihe Yang, Bingyi Kang, Zilong Huang, Zhen Zhao, Xiaogang Xu, Jiashi Feng, and Hengshuang Zhao. Depth anything v2. *arXiv:2406.09414*, 2024. 1, 3
- [65] Kaixin Yao, Longwen Zhang, Xinhao Yan, Yan Zeng, Qixuan Zhang, Lan Xu, Wei Yang, Jiayuan Gu, and Jingyi Yu. Cast: Component-aligned 3d scene reconstruction from an rgb image, 2025. 1, 3, 8
- [66] Chongjie Ye, Yushuang Wu, Ziteng Lu, Jiahao Chang, Xiaoyang Guo, Jiaqing Zhou, Hao Zhao, and Xiaoguang Han. Hi3dgen: High-fidelity 3d geometry generation from images via normal bridging. *arXiv preprint arXiv:2503.22236*, 2025. 7
- [67] Xu Yinghao, Shi Zifan, Yifan Wang, Chen Hansheng, Yang Ceyuan, Peng Sida, Shen Yujun, and Wetzstein Gordon. Grm: Large gaussian reconstruction model for efficient 3d reconstruction and generation, 2024. 3
- [68] Chong Zeng, Yue Dong, Pieter Peers, Hongzhi Wu, and Xin Tong. Renderformer: Transformer-based neural rendering of triangle meshes with global illumination. In *ACM SIGGRAPH 2025 Conference Papers*, 2025. 5
- [69] Jason Y Zhang, Amy Lin, Moneish Kumar, Tzu-Hsuan Yang, Deva Ramanan, and Shubham Tulsiani. Cameras as rays: Pose estimation via ray diffusion. *arXiv preprint arXiv:2402.14817*, 2024. 4, 5
- [70] Longwen Zhang, Ziyu Wang, Qixuan Zhang, Qiwei Qiu, Anqi Pang, Haoran Jiang, Wei Yang, Lan Xu, and Jingyi Yu. Clay: A controllable large-scale generative model for creating high-quality 3d assets. *ACM Transactions on Graphics (TOG)*, 43(4):1–20, 2024. 1, 3

- [71] Shangzhan Zhang, Jianyuan Wang, Yinghao Xu, Nan Xue, Christian Rupprecht, Xiaowei Zhou, Yujun Shen, and Gordon Wetzstein. Flare: Feed-forward geometry, appearance and camera estimation from uncalibrated sparse views, 2025. [3](#)
- [72] Zibo Zhao, Zeqiang Lai, Qingxiang Lin, Yunfei Zhao, Haolin Liu, Shuhui Yang, Yifei Feng, Mingxin Yang, Sheng Zhang, Xianghui Yang, et al. Hunyuan3d 2.0: Scaling diffusion models for high resolution textured 3d assets generation. *arXiv preprint arXiv:2501.12202*, 2025. [1](#)
- [73] Jensen (Jinghao) Zhou, Hang Gao, Vikram Voleti, Aaryaman Vasishtha, Chun-Han Yao, Mark Boss, Philip Torr, Christian Rupprecht, and Varun Jampani. Stable virtual camera: Generative view synthesis with diffusion models. *arXiv preprint arXiv:2503.14489*, 2025. [3](#)

A. Appendix

A.1. Implementation

Dataset. We train our model using several datasets, including ABO [6], HSSD [21], 3D-FUTURE [10], and a subset of Objaverse-XL [7], totaling approximately 260K 3D assets. These artist-curated datasets are predominantly aligned to a canonical frame where the ground plane corresponds to $z = 0$. Following TRELIS [59], we encode each asset into occupancy grids and structured latents that are suitable for training the flow transformer. The structured latents can be decoded into high-quality triangle meshes or Gaussian splats using the SLat decoders. To enable diverse camera generation, we render 24 conditioning images from random viewpoints for each asset, with augmented focal lengths ranging from 24 mm to 200 mm.

Pose Encoding and Recovery. Following the methodology outlined in the main text, we represent the camera pose and coarse scene geometry as a voxelized 3D occupancy grid paired with a UV coordinate volume, denoted as $\{\mathbf{x}_i, \mathbf{u}_i(\boldsymbol{\theta})\}_{i=1}^L$. To facilitate efficient learning, we employ a 3D VAE to compress the input UV volume (resolution 64^3) into a compact latent representation (resolution 16^3). These pose latents are concatenated with occupancy embeddings to condition the training of the structural flow model, \mathcal{G}_S . For pose recovery, the latents generated by \mathcal{G}_S are decoded back into the UV volume. We then estimate the camera extrinsics $[\mathbf{R}|\mathbf{t}]$ and intrinsics \mathbf{K} using the Perspective-n-Point (PnP) algorithm in Algo. 1. We evaluate the fidelity of this reconstruction in Tab. 5, reporting the mean and 95th percentile for Reprojection Error in normalized pixel coordinates, Relative Translation Error (RTE), Relative Rotation Error (RRE), and Relative Field-of-View (RFov) error in degrees. With the solved camera pose, we finally train the latent flow model \mathcal{G}_L to synthesize the structured features $\{\mathbf{f}_i\}_{i=1}^L$ conditioned on the occupancy and the pose-aligned visual features.

Table 5. **Pose Reconstruction Fidelity.** We evaluate the accuracy of camera poses recovered from the decoded UV volumes via the PnP algorithm. We report the Reprojection Error in normalized pixels, RRE, RTE, and RFov in degrees.

Metric	Reproj. Err.	RRE	RTE	RFov
Mean	0.0009	0.46	0.45	0.15
95% Quantile	0.0011	1.14	1.14	0.31

Training Details. We initialize our models using the pre-trained weights of TRELIS. During training, we apply classifier-free guidance [14] (CFG) with a drop rate of 0.1. Both \mathcal{G}_S and \mathcal{G}_L are trained using AdamW [30] at a fixed

Algorithm 1 Perspective-n-Point solver via Direct Linear Transformation (DLT)

\mathcal{X} : Sets of 3D coordinates $\{\mathbf{x}_i\}_{i=1}^N$

\mathcal{U} : 2D coordinates $\{\mathbf{u}_i\}_{i=1}^N$

```

 $N \leftarrow |\mathcal{X}|$  ▷ Number of correspondences
 $\mathbf{A} \leftarrow \mathbf{0}_{2N \times 12}$  ▷ Initialize coefficient matrix
for  $i = 1$  to  $N$  do
     $\tilde{\mathbf{x}}_i \leftarrow [\mathbf{x}_i^\top, 1]^\top$  ▷ Homogeneous coordinates
     $u_i, v_i \leftarrow \mathbf{u}_i$ 
     $\mathbf{A}[2i - 1, :] \leftarrow [\tilde{\mathbf{x}}_i^\top, \mathbf{0}^\top, -u_i \tilde{\mathbf{x}}_i^\top]$ 
     $\mathbf{A}[2i, :] \leftarrow [\mathbf{0}^\top, \tilde{\mathbf{x}}_i^\top, -v_i \tilde{\mathbf{x}}_i^\top]$ 
end for
 $[\mathbf{U}, \boldsymbol{\Sigma}, \mathbf{V}^\top] \leftarrow \text{SVD}(\mathbf{A})$ 
 $\mathbf{p} \leftarrow \mathbf{V}[:, -1]$  ▷ Solution is the last column of  $\mathbf{V}$ 
 $\mathbf{P} \leftarrow \text{reshape}(\mathbf{p}, 3, 4)$  ▷ Camera matrix  $\mathbf{P} \in \mathbb{R}^{3 \times 4}$ 
if  $\det(\mathbf{P}_{1:3, 1:3}) < 0$  then ▷ Fix scale/sign ambiguity
     $\mathbf{P} \leftarrow -\mathbf{P}$ 
end if
 $[\mathbf{K}, \mathbf{R}, \mathbf{t}] \leftarrow \text{RQ}(\mathbf{P})$  ▷ Decompose camera matrix
return  $\mathbf{K}, \mathbf{R}, \mathbf{t}$ 

```

learning rate of 1×10^{-4} for 500k and 100k steps, respectively. Training completes in approximately one week on 32 GPUs. At inference, we use 25 sampling steps with classifier-free guidance strengths of 7.5 and 3.0 for \mathcal{G}_S and \mathcal{G}_L , respectively.

A.2. Occlusion-aware conditioning

To handle occlusion in complex scene reconstruction, our model leverages partial 3D object observations as conditions to generate complete objects. Our model takes a 2D occlusion mask $\mathbf{M}^{\text{occ}} \in \{0, 1\}^{H \times W}$ as input alongside the visible object observation \mathbf{I}^{cond} . The mask \mathbf{M}^{occ} identifies pixels that may belong to the object if occluders were removed, with values set to zero when no occlusion is present. Together, \mathbf{M}^{occ} and the alpha channel of \mathbf{I}^{cond} identify three pixel classes: (a) directly observed object pixels, (b) background pixels that must not contain the object, and (c) occluded pixels that may or may not contain the object.

We apply two modifications to both flow transformers to incorporate the mask. First, inspired by Amodal3R [58], we modulate the attention weight matrix during global condition injection via cross-attention using the mask. Specifically, the attention weight for each input token is computed by patching the mask to match the DINOv2 tokens and calculating the ratio of unmasked pixels in each patch. The logarithm of the weight values is added to the attention logits before applying the softmax operation. Second, for the geometry and appearance flow model that takes additional pose-aligned features, we concatenate the input image with the mask as an additional channel before feeding it into the convolution layer in the second stage.

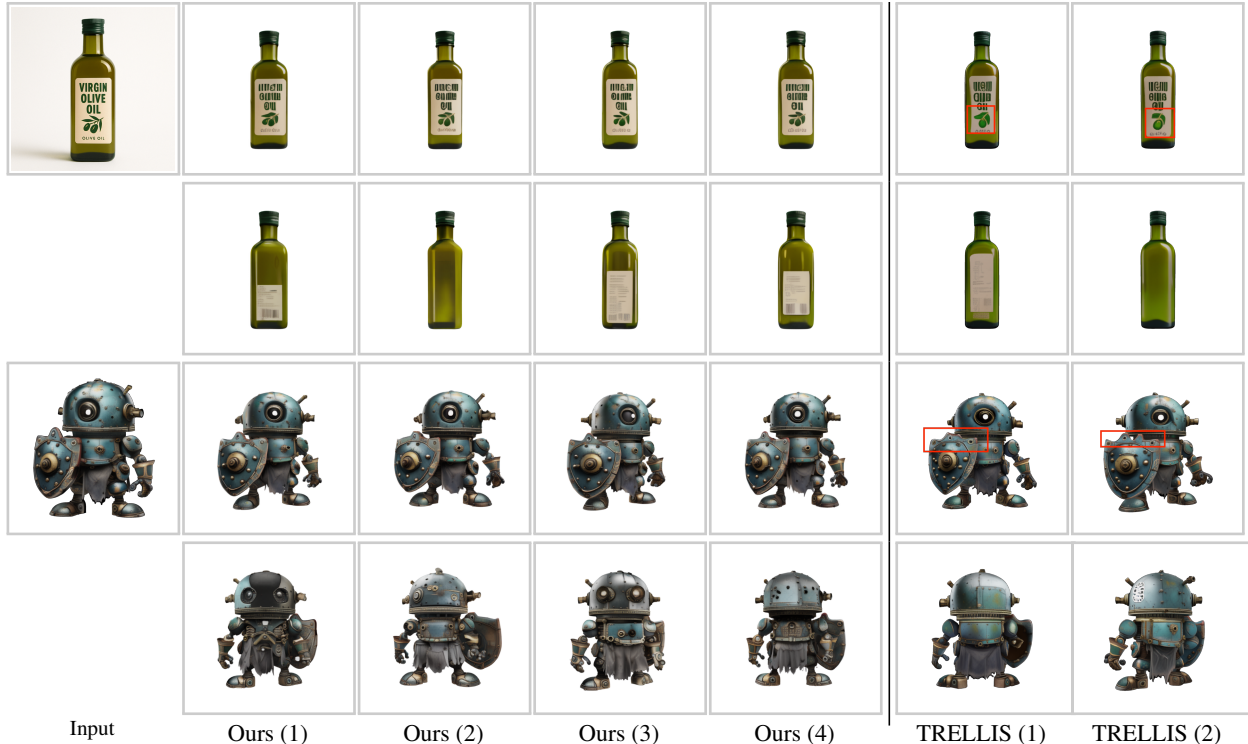


Figure 8. **Diversity of our Generative Reconstruction.** We visualize canonical front and back views of generated 3D objects using random seeds (1-4). Given a single input image, our model synthesizes diverse hypotheses for unobserved regions while remaining highly consistent with visible regions. In contrast, the base 3D generator [59] struggles to conform to the input image, or produce less diverse unobserved regions.

During training, we randomly generate occlusion masks M^{occ} following Amodal3R and zero out the corresponding regions in I^{cond} , preventing information leakage on occlusion regions and encouraging the model to reconstruct complete 3D objects from partial observations. At inference time, occlusion masks can be obtained heuristically or manually for scene reconstruction.

A.3. Generative reconstruction diversity.

Reconstruction methods like LRM [16] typically generate a single 3D object from one image. However, our approach not only surpasses LRM in terms of reconstruction quality but also produces multiple plausible interpretations—what we refer to as generative reconstruction. Since standard metrics do not effectively capture this diversity, we offer qualitative comparisons in Figure 8. The results demonstrate that our framework creates diverse 3D models with visible regions that consistently align with the input image. In contrast, conventional 3D generation methods [59] often struggle to maintain consistency in the visible regions of the objects they create. Furthermore, while directly processing an image with multiple objects may still yield a scene, the generation quality is often degraded as such inputs are out-of-distribution. In contrast, our method allows for component-aligned compositional reconstruction,

as demonstrated by the additional examples in Figure 10.

A.4. Qualitative comparison with 3D generators

Since TRELLIS [59] does not provide an explicit object-centric camera pose for the input image and post-hoc alignment is unreliable, we cannot conduct fair quantitative evaluation of reprojection consistency. We therefore focus on qualitative comparisons in Figure 9. For both methods, we render canonical object from front and back views. As shown, TRELLIS struggles to maintain texture consistency with the input image, exhibiting notable color drifting on the candle statue, teddy bear, and the lamb. In contrast, our method closely preserves the appearance of input. Importantly, although we incorporate pixel-level cues via back-projection, the model does not simply copy pixels: the generated back views remain coherent with the front, indicating learned view-consistent geometry and appearance. These results demonstrate that our mechanism effectively mitigates color drifting and texture inconsistency. We hypothesize that this limitation is common among 3D generators that lack localized, pixel-attended conditioning, including follow-up works of TRELLIS. We hope these findings can inspire future designs of 3D generators.

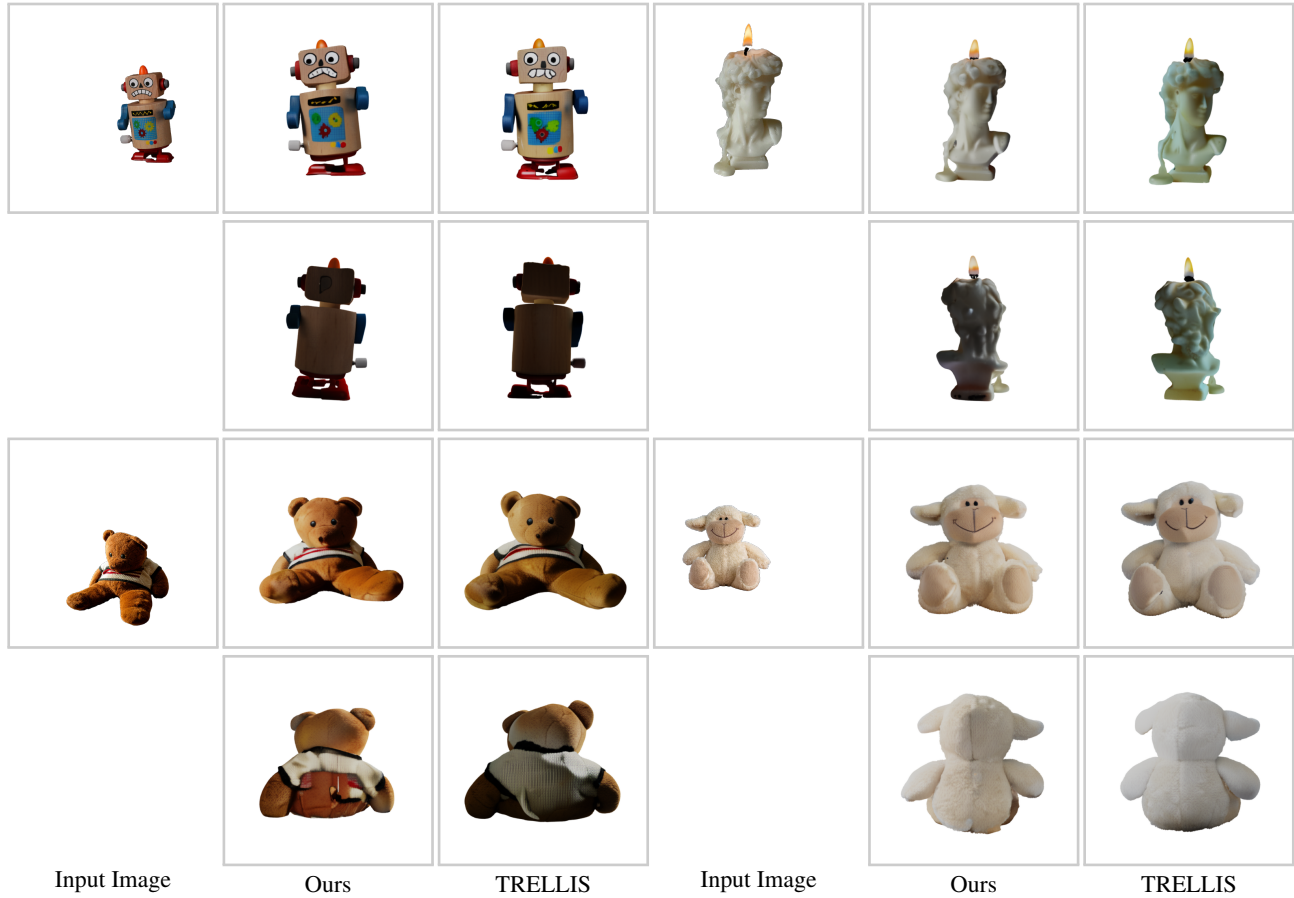


Figure 9. **Qualitative comparison: Generative Reconstruction vs. 3D Generation.** Unlike standard 3D generation, which aims to create novel objects from images, our generative reconstruction is specifically designed to accurately recreate a particular object that replicates the visible regions of the input image while maintaining diversity in the invisible regions. This difference in objectives is crucial, as prior 3D generators [59] are not optimized for this task and often produce artifacts such as *color drift* and *texture inconsistencies*. As demonstrated in the canonical front and back views, our method’s pose-aligned image conditioning effectively reduces these issues, resulting in a reconstruction that remains true to the input.



Figure 10. **Additional examples of component-aligned scene reconstruction.** For each example shown, the panels display: (top left) the input image, (top right or bottom left) the final rendered output, and (bottom) the reconstructed individual components, color-coded for clarity.